

Classical molecular-dynamics potential for the mechanical strength of nanocrystalline composite fcc Al+ α -Fe₂O₃

Vikas Tomar^{1,*} and Min Zhou^{2,†}

¹*Department of Aerospace and Mechanical Engineering, University of Notre Dame, Notre Dame, Indiana 46556, USA*

²*George W. Woodruff School of Mechanical Engineering, Georgia Institute of Technology, Atlanta, Georgia 30332, USA*

(Received 3 February 2006; revised manuscript received 12 April 2006; published 26 May 2006)

A classical molecular-dynamics potential for analyzing mechanical deformation in the α -Fe₂O₃+fcc-Al material system is developed. The potential includes an embedded atom method cluster functional, a Morse-type pair function, and a second-order electrostatic interaction function. It is fitted to the lattice constants, elastic constants, and cohesive energies of fcc Al, bcc Fe, α -Fe₂O₃, α -Al₂O₃, and B2-FeAl, accounting for the fact that mixtures of Al and Fe₂O₃ are chemically reactive and deformation may cause the formation of these components as reaction products or intermediates. To obtain close approximations of the behavior of mixtures with any combination of the atomic elements, the potential is formulated and fitted such that the Al-Al, Fe-Fe, Al-Fe, O-O, Fe-O, and Al-O interactions are accounted for in an explicit and interdependent manner. In addition to being fitted to the lattice constants, elastic constants, and cohesive energies, the potential gives predictions of the surface and stacking fault energies for the crystalline components that compare well with the predictions of established potentials in the literature for the corresponding crystalline components. The potential is applied to analyze quasistatic tensile deformation in nanocrystalline Al, in nanocrystalline Fe₂O₃, and in nanocrystalline Al+Fe₂O₃ composites. Application of the potential to nanocrystalline Al reveals the features of mechanical deformation, such as the formation of unit dislocations, flow strength approaching ideal shear strength, and the Hall-Petch relationships, that are in close agreement with experiments and with the predictions of established potentials for Al in the literature. Analyses of deformation in nanocrystalline Fe₂O₃ and in nanocrystalline Al+Fe₂O₃ composites point to the possibility that the strength of the nanocomposites can only be calculated using the mixture theory if the average grain size is above a critical value. Below the critical grain size, an accurate account of interfacial stresses is important to the prediction of the strength. For composites with grain sizes above the critical value, the observed dependence of strength on volume fraction is in agreement with experimental observations.

DOI: [10.1103/PhysRevB.73.174116](https://doi.org/10.1103/PhysRevB.73.174116)

PACS number(s): 62.25.+g, 34.20.Cf

I. INTRODUCTION

Molecular-dynamics (MD) simulations are an important tool for analyzing the thermomechanical behavior of materials and have been widely used for single-phase materials, e.g., Buehler *et al.*,¹ partly because of readily available atomic potentials for such systems. One of the primary focuses of recent development in materials research is the synthesis of multicomponent materials in order to achieve multifunctionality. Fe₂O₃+Al nanocomposites synthesized through a sol-gel process are one example that offers the promise of combined chemical reactivity and mechanical strength when mixed with appropriate nanoscopic reinforcements such as epoxy.² The analyses of such composite material systems, however, require more complex potentials which are often not available. Consequently, there is a strong need for developing interatomic potentials for material systems consisting of more than one component.

This research focuses on the development of an interatomic potential for describing mechanical deformation in α -Fe₂O₃+fcc-Al nanocomposites which are chemically active ThermiteTM mixtures. Obviously, the possibility of the formation of Al₂O₃, Fe, and other intermediate states needs to be considered. Therefore, the potential is required to simultaneously describe the behavior of α -Fe₂O₃, fcc Al, α -Al₂O₃, and bcc Fe. To state it differently, Al-Al, Fe-Fe, Al-Fe, Al-O, Fe-O, and O-O interactions and the coupling

between these interactions must be accounted for. This task necessitates a functional form that allows multibody, pairwise, and electrostatic interactions among different species to be described. Our approach here is to first fit the potential parameters for the Al-Al, Fe-Fe, Al-O, Fe-O, and O-O interactions to the lattice constants, elastic moduli, and cohesive energies of fcc Al, bcc Fe, α -Fe₂O₃, and α -Al₂O₃. To determine the Fe-Al parameters, the potential is then fitted to the lattice constants and cohesive energies of B2-FeAl. Consequently, the potential is capable of simultaneously describing the crystalline properties of fcc Al, bcc Fe, B2-FeAl, α -Fe₂O₃, and α -Al₂O₃. With this relatively general applicability, we surmise that the potential provides reasonable approximations of the Al-Al, Fe-Fe, Al-Fe, Al-O, Fe-O, and O-O interactions and their coupling in the presence of each other as may exist in a general system with a combination of these components.

Both α -Fe₂O₃ and α -Al₂O₃ belong to a family of scale-nohedral hexagonal (trigonal) crystals, cf. Wyckoff.³ These oxides can be characterized as having mixed ionic and covalent bonds. Interatomic potentials for these oxides have been developed following fully ionic descriptions, e.g., Mackrodt and Stewart⁴ and Gale *et al.*;⁵ embedded atom method (EAM)-based approaches, e.g., Baskes,⁶ Strietz and Mintmire,⁷ and Ohira and Inoue,⁸ density functional-based approaches, e.g., Kenny *et al.*;⁹ and mixed covalent-ionic descriptions, e.g., Belashchenko and Ostravski.¹⁰ Al, Fe,

and B2-FeAl are parts of the cubic family of crystals. Potentials for Al have been described by Foiles *et al.*,¹¹ Voter and Chen,¹² Baskes,⁶ and Mishin *et al.*¹³ Among these, the MEAM-based formulation of Baskes⁶ has the smallest cutoff range, i.e., only nearest neighbor interactions are considered. This potential has been recently modified by Baskes *et al.*¹⁴ based on *ab initio* results to more accurately predict the stacking fault energy and surface energy of Al. Interatomic potentials for Fe have been developed by Pasianot *et al.*,¹⁵ Baskes,⁶ Simonelli *et al.*,¹⁶ and Farkas *et al.*¹⁷ Among these potentials, the model of Farkas *et al.*¹⁷ takes into account both *ab initio* and experimental data. Potential models for Fe-Al intermetallic systems have been developed by Besson and Morillo¹⁸ and Vailhe and Farkas.¹⁹ The model of Besson and Morillo¹⁸ is fitted to a wider range of properties and is widely applicable. In our research here, the functional form is a combination of the EAM functional by Foiles *et al.*,¹¹ the pair function by Besson and Morillo,¹⁸ and the second-order electrostatic function by Strietz and Mintmire.⁷

One requirement for a multicomponent interatomic potential is that it prescribes a smooth transition of structure at the interface between two different crystalline regions. For example, Al close to Fe₂O₃ can be oxidized to form an Al_pO_q structure or it can bond with Fe to form an Al_xFe_y structure. Two commonly used approaches to achieve such transition are (1) the Tersoff bond-order potential, cf. Tersoff,²⁰ and (2) the electrostatics (ES) +EAM model of Strietz and Mintmire.⁷ The Tersoff bond-order potential was initially used to model phases of silicon and was later extended to describe hydrocarbon systems by Brenner²¹ in the form of the Brenner reactive bond-order potential (REBO). The latest variation in this scheme is the generalized extended empirical bond-order dependent (GEEBOD) potential with a functional representation of the van der Waals interactions and the electrostatic interactions, see Che *et al.*²² The ES +EAM model has been used by Kalia *et al.*²³ to analyze pressure-induced reactions between aluminum and oxygen under quasistatic conditions. This model uses the principle of electronegativity equalization, see Mortier *et al.*²⁴ and Rappe and Goddard III,²⁵ to determine the local-environment-dependent charge of an atom. It is ideally suited for the description of systems which have primarily mixed ionic-covalent bonding. Similar approaches are taken by Rick *et al.*²⁶ for polar systems, by Liu *et al.*²⁷ for a new *ab initio* water potential, and by Goddard III *et al.*²⁸ for pressure-induced phase transformation in ferroelectrics. In the current work, a modified ES+EAM term is included in the potential for describing the transition from one crystal system to the other at the interfaces between a metallic system such as Al and an ionic-covalent system such as Fe₂O₃.

II. FUNCTIONAL FORM OF THE INTERATOMIC POTENTIAL

The functional form of the potential is a combination of existing potentials in the literature for the individual crystalline components, i.e.,

$$E^{total}(\mathbf{r}, q) = \left\{ \sum_i F_i \left(\sum_j [\rho_j(r_{ij})] \right) + \frac{1}{2} \left(\sum_i \sum_j \phi_{ij}(r_{ij}) \right)_{i \neq j} \right\}_{glue} + \left\{ \sum_i E_{es}(\mathbf{r}_i, q_i) \right\}_{electrostatic}. \quad (1)$$

In the above expression, \mathbf{r}_i is the position vector of atom i and r_{ij} is the distance between atoms i and j . This potential expression contains a glue potential term (E_{glue}) similar to the EAM potential with a generalized cluster functional (cf. Carlsson²⁹) and an electrostatic potential term (E_{es}) for second-order electrostatic interactions. The electrostatic interactions are considered for point charges located at atomic core centers as well as for diffused charges around the atomic cores. Specifically, for each atomic species (Al, Fe, or O) the total energy is a function of atomic position vector \mathbf{r} and charges q in the form

$$E(\mathbf{r}, q) = E_{glue}(\mathbf{r}) + E_{es}(\mathbf{r}, q). \quad (2)$$

Here,

$$E_{glue}(\mathbf{r}) = \sum_i F_i \left(\sum_j \rho_j \right) + \frac{1}{2} \sum_{i,j(i \neq j)} \phi_{ij} \quad (3)$$

is the glue potential with a generalized cluster functional $F(\sum_j \rho_j)$ and a pair interaction potential ϕ_{ij} . The form of $F(\sum_j \rho_j)$ is chosen as

$$F \left(\sum_j \rho_j \right) = E_0 A \left[\sum_j \rho_j \ln \left(\sum_j \rho_j \right) \right]^B. \quad (4)$$

In the above expression, E_0 , A , and B are fitting parameters (they are different for Al, Fe, and O) and ρ is the embedding electron density (see Baskes⁶) whose functional form is taken to be the same as that used by Foiles *et al.*¹¹ The pair interaction function $\phi_{ij}(r_{ij})$ is based on that used by Besson and Morillo¹⁸ for Fe-Al alloys, i.e.,

$$\phi_{ij}(r) = \psi_{ij}(r_{ij}) - \psi_{ij}(D_p) + \frac{D_p}{20} \left[1 - \left(\frac{r_{ij}}{D_p} \right)^{20} \right] \psi'_{ij}(D_p) \quad (5)$$

for $r_{ij} < D_p$.

Note that the interaction goes to zero smoothly at the cutoff distance $D_p \cdot \psi_{ij}(r_{ij})$ in the above expression is taken as

$$\psi_{ij}(r_{ij}) = \psi_0 \{ \exp[-2\gamma(r_{ij} - t)] - 2 \exp[-\gamma(r_{ij} - t)] \}. \quad (6)$$

Here, γ , ψ_0 , and t are parameters to be determined through fitting (they are different for Al-Al, Fe-Fe, Al-Fe, Al-O, Fe-O, and O-O pairs). The electrostatic term in Eq. (2) is

$$\sum_i E_{es}(\mathbf{r}_i, q_i) = \sum_i q_i \chi_i + \frac{1}{2} \sum_{i,j(i \neq j)} q_i q_j V_{ij}. \quad (7)$$

Here, χ is the instantaneous electronegativity and V is the electrostatic pair interaction potential. $E_{es}(\mathbf{r}, \mathbf{q})$ includes point charge interactions as well as interactions among charges distributed around the centers of atomic cores. For simplicity, the charge distributions are taken to be spherical. The expression for $E_{es}(\mathbf{r}, q)$ is obtained by describing the energy $E_i(q_i)$ of a neutral atom i as a Taylor series in its valence charge q_i (see Rappe and Goddard III²⁵), i.e.,

$$E_i(q_i) = E_i(0) + \chi_i^0 q_i + \frac{1}{2} J_i^0 q_i^2. \quad (8)$$

The first derivative χ_i^0 on the right-hand side is denoted as the electronegativity, see Mortier *et al.*²⁴ The second derivative J_i^0 has been associated with atomic hardness, see Parr and Pearson,³⁰ or with self-Coulomb repulsion, see Rappe and Goddard III.²⁵ The electrostatic energy $E_{es}(\mathbf{r}, q)$ of a set of interacting atoms with atomic charges q_i is the sum of the atomic energies E_i and the electrostatic interaction energies between all pairs of atoms, i.e.,

$$\begin{aligned} \sum_i E_{es}(\mathbf{r}_i, q_i) &= \sum_i E_i(q_i) + \frac{1}{2} \sum_{i,j(i \neq j)} V_{ij}(r_{ij}; q_i, q_j) \\ &= \sum_i \left(E_i(0) + \chi_i^0 q_i + \frac{1}{2} J_i^0 q_i^2 \right) + \frac{1}{2} \sum_{i,j(i \neq j)} \\ &\quad \times \left[\int d^3 \mathbf{r}_1 \int d^3 \mathbf{r}_2 \rho_i(\mathbf{r}_1; \mathbf{r}_i, q_i) \rho_j(\mathbf{r}_2; \mathbf{r}_j, q_j) / r_{12} \right]. \end{aligned} \quad (9)$$

Here, the second term on the right-hand side describes electrostatic interactions, with $\rho_i(\mathbf{r}_1; \mathbf{r}_i, q_i)$ being the charge distribution in a spherical volume defined by position vector \mathbf{r}_1 around atom i with total charge q_i . \mathbf{r}_{12} in the above expression defines a volume that results from the intersection of two spherical volumes with radii \mathbf{r}_1 and \mathbf{r}_2 . The form used for $\rho_i(\mathbf{r}_1; \mathbf{r}_i, q_i)$ is given by Strietz and Mintmire,⁷ i.e.,

$$\rho_i(\mathbf{r}_1; \mathbf{r}_i, q_i) = Z_i \delta(\mathbf{r}_1 - \mathbf{r}_i) + (q_i - Z_i) f_i(\mathbf{r}_1 - \mathbf{r}_i). \quad (10)$$

Here, Z_i is the *effective* nuclear point charge which must satisfy the condition $0 < Z_i < Z_a$, with Z_a being the total

nuclear charge of the species to which atom i belongs (Al, Fe, or O). Function f_i describes the radial distribution of the valence charges in space. It is chosen to be in the Gaussian form to correspond to the Slater $1s$ orbital with a parameter ξ_i , i.e.,

$$f_i(r) = \frac{\xi_i^3}{\pi} \exp(-2\xi_i r). \quad (11)$$

Placing $\rho_i(\mathbf{r}_1; q_i)$ from Eq. (10) in Eq. (9) leads to

$$\begin{aligned} \sum_{i,j(i \neq j)} V_{ij}(r_{ij}; q_i, q_j) &= \sum_i \sum_{j(i \neq i)} \{ q_i q_j [f_i | f_j] + q_i Z_j ([j | f_i] - [f_i | f_j]) \\ &\quad + q_j Z_i ([i | f_j] - [f_i | f_j]) + Z_i Z_j ([f_i | f_j] \\ &\quad - [i | f_j] - [j | f_i] + 1/r_{ij}) \}. \end{aligned} \quad (12)$$

Here,

$$[f_i | f_j] = \int d^3 \mathbf{r}_1 \int d^3 \mathbf{r}_2 \frac{f_i(\mathbf{r}_1) f_j(\mathbf{r}_2)}{r_{12}} \quad (13)$$

is the two-center Coulomb interaction integral between f_i and f_j and

$$[j | f_i] = \int d^3 \mathbf{r} \frac{f_i(\mathbf{r})}{|\mathbf{r} - \mathbf{r}_j|} \quad (14)$$

is the nuclear attraction integral. The integration in the above equations can be easily calculated using prolatiorial spheroidal coordinates, see Roothan.³¹ The expressions for these integrals are

$$[j | f_i] = \frac{1}{r_{ij}} \{ 1 - [(1 + \xi_i r_{ij}) \exp(-2\xi_i r_{ij})] \}, \quad (15)$$

and

$$[f_i | f_j] = \begin{cases} \frac{1}{r_{ij}} \left\{ 1 - \left(1 - \frac{\xi_i^2 + \xi_j^2}{\xi_i^2 - \xi_j^2} \right) \left\{ \frac{1}{4} \left[2 + \frac{\xi_i^2 + \xi_j^2}{\xi_i^2 - \xi_j^2} \right] + \frac{1}{4} \xi_i r_{ij} \right\} \exp(-2\xi_i r_{ij}) - \right. \\ \left. \left(1 + \frac{\xi_i^2 + \xi_j^2}{\xi_i^2 - \xi_j^2} \right) \left\{ \frac{1}{4} \left[2 - \frac{\xi_i^2 + \xi_j^2}{\xi_i^2 - \xi_j^2} \right] + \frac{1}{4} \xi_j r_{ij} \right\} \exp(-2\xi_j r_{ij}) \right\} & \text{if } \xi_i \neq \xi_j \\ \frac{1}{r_{ij}} \left\{ 1 - \left[1 + \frac{11}{8} (\xi_i r_{ij}) + \frac{3}{4} (\xi_i r_{ij})^2 + \frac{1}{6} (\xi_i r_{ij})^3 \right] \exp(-2\xi_i r_{ij}) \right\} & \text{if } \xi_i = \xi_j. \end{cases} \quad (16)$$

Equations (9) and (12) can be combined to yield

$$\begin{aligned} E_{es} &= \sum_i (E_i(0) + q_i \chi_i) + \frac{1}{2} \sum_{i,j(i \neq j)} \{ q_i Z_j ([j | f_i] - [f_i | f_j]) \\ &\quad + q_j Z_i ([i | f_j] - [f_j | f_i]) \} + \frac{1}{2} \sum_i q_i^2 J_i^0 + \frac{1}{2} \sum_{i,j(i \neq j)} \{ q_i q_j [f_i | f_j] \\ &\quad + Z_i Z_j ([f_i | f_j] - [i | f_j] - [j | f_i] + 1/r_{ij}) \}. \end{aligned} \quad (17)$$

The above expression can be simplified and expressed as

$$E_{es} = E_0 + \sum_i q_i \chi_i + \frac{1}{2} \sum_{i,j(i \neq j)} q_i q_j E_{ij}, \quad (18)$$

such that

$$E_0 = \sum_i E_i(0) + \frac{1}{2} \sum_{i,j(i \neq j)} Z_i Z_j ([f_i|f_j] - [i|f_j] - [j|f_i] + 1/r_{ij}) \quad (19)$$

defines the ground state energy,

$$\chi_i = \chi_i^0 + \sum_{i,j(j \neq i)} Z_j ([j|f_i] - [i|f_j]) = \chi_i^0 + \sum_{i,j(j \neq i)} Z_j \left(\int d^3\mathbf{r} \frac{f_i(\mathbf{r})}{|\mathbf{r} - \mathbf{r}_i|} - \int d^3\mathbf{r}_1 \int d^3\mathbf{r}_2 \frac{f_i(\mathbf{r}_1) f_j(\mathbf{r}_2)}{\mathbf{r}_{12}} \right) \quad (20)$$

defines the instantaneous electronegativity, and

$$E_{ij} = \begin{cases} J_i^0 & i = j \\ \int d^3\mathbf{r}_1 \int d^3\mathbf{r}_2 \frac{f_i(\mathbf{r}_1) f_j(\mathbf{r}_2)}{\mathbf{r}_{12}} & i \neq j \end{cases} \quad (21)$$

defines the electrostatic interactions in the system. The exponential form of f leads the integrals in the above equations to decompose into a leading $1/r_{ij}$ term and an additional term to exponentially decay as a function of r_{ij} . All lattice sums, therefore, can be decomposed into terms involving $1/r_{ij}$ and terms which are exponentially damped. The long range terms cancel each other out in Eq. (20), leaving only $1/r_{ij}$ terms in the expression for E_{ij} in Eq. (21). The reduced expression is

$$\chi_i = \chi_i^0 + \sum_{j \neq i} \frac{Z_j}{r_{ij}} \left\{ \begin{array}{l} -[(1 + \xi_i^s r_{ij}) \exp(-2\xi_i^s r_{ij})] + \\ \left(1 - \frac{\xi_i^2 + \xi_j^2}{\xi_i^2 - \xi_j^2}\right) \left\{ \frac{1}{4} \left[2 + \frac{\xi_i^2 + \xi_j^2}{\xi_i^2 - \xi_j^2} \right] + \frac{1}{4} \xi_i r_{ij} \right\} \exp(-2\xi_i r_{ij}) + \\ \left(1 + \frac{\xi_i^2 + \xi_j^2}{\xi_i^2 - \xi_j^2}\right) \left\{ \frac{1}{4} \left[2 - \frac{\xi_i^2 + \xi_j^2}{\xi_i^2 - \xi_j^2} \right] + \frac{1}{4} \xi_j r_{ij} \right\} \exp(-2\xi_j r_{ij}) \end{array} \right\} \quad \text{if } \xi_i \neq \xi_j$$

$$\left\{ \begin{array}{l} -[(1 + \xi_i^s r_{ij}) \exp(-2\xi_i^s r_{ij})] + \\ \left[1 + \frac{11}{8} (\xi_i r_{ij}) + \frac{3}{4} (\xi_i r_{ij})^2 + \frac{1}{6} (\xi_i r_{ij})^3 \right] \exp(-2\xi_i r_{ij}) \end{array} \right\} \quad \text{if } \xi_i = \xi_j . \quad (22)$$

for χ_i and

$$E_{ij} = \left\{ \begin{array}{l} \frac{1}{r_{ij}} \left\{ \begin{array}{l} 1 - \left(1 - \frac{\xi_i^2 + \xi_j^2}{\xi_i^2 - \xi_j^2}\right) \left\{ \frac{1}{4} \left[2 + \frac{\xi_i^2 + \xi_j^2}{\xi_i^2 - \xi_j^2} \right] + \frac{1}{4} \xi_i r_{ij} \right\} \exp(-2\xi_i r_{ij}) - \\ \left(1 + \frac{\xi_i^2 + \xi_j^2}{\xi_i^2 - \xi_j^2}\right) \left\{ \frac{1}{4} \left[2 - \frac{\xi_i^2 + \xi_j^2}{\xi_i^2 - \xi_j^2} \right] + \frac{1}{4} \xi_j r_{ij} \right\} \exp(-2\xi_j r_{ij}) \end{array} \right\} \quad \text{if } \xi_i \neq \xi_j, \\ \frac{1}{r_{ij}} \left\{ 1 - \left[1 + \frac{11}{8} (\xi_i r_{ij}) + \frac{3}{4} (\xi_i r_{ij})^2 + \frac{1}{6} (\xi_i r_{ij})^3 \right] \exp(-2\xi_i r_{ij}) \right\} \quad \text{if } \xi_i = \xi_j, \end{array} \right. \quad (23)$$

for E_{ij} . In Eq. (19), E_0 depends only on the nuclear charges and does not depend on charges q_i . Correspondingly, E_0 is not accounted for separately during energy calculations. This term is considered to be included in the glue part E_{glue} of the interatomic potential which consists of a volume-dependent many-body term accounting for the ground state zero charge energy and a term accounting for the effective pair interactions. Overall, the parameters needed to completely specify the potential are

(1) A, B, r_0, β, t , and cutoff distance D_p for describing the density functional and cluster function for each of Al, Fe, and O (a subtotal of $3 \times 6 = 18$ parameters);

(2) D_p, ψ_0, γ , and t_k for describing each of the Al-Al, Al-Fe, Fe-Fe, O-O, Al-O, and Fe-O effective pair interactions (a subtotal of $6 \times 4 = 24$ parameters); and

(3) ξ (Gaussian charge distribution parameter), Z (core charge), χ_0, J_0 , and the short range electrostatic cutoff radius (r_{ES}) for exponentially decaying terms of the interatomic potential for specifying the electrostatic energy of Al, O, and Fe atoms (a subtotal of $3 \times 5 = 15$ parameters).

The total number of parameters is 57. Based on the above description, for an Al+Fe₂O₃ nanocomposite structure, the interatomic potential has (in the following, α stands for one of the Al, Fe, or O species)

$$\begin{aligned}
 E_{ES}^\alpha = q_\alpha \left\{ \chi_\alpha^0 + \sum_{i(\text{Al}), j(\neq i)} Z_j \left[\int d^3\mathbf{r} \frac{f_\alpha(\mathbf{r})}{|\mathbf{r}-\mathbf{r}_j|} - \int d^3\mathbf{r}_1 \int d^3\mathbf{r}_2 \frac{f_\alpha(\mathbf{r}_1)f_j(\mathbf{r}_2)}{\mathbf{r}_{12}} \right] \right\} + \frac{1}{2} \left\{ \sum_{i(\kappa)} q_\alpha^2 J_\alpha^0 \right. \\
 \left. + \sum_{i(\kappa), j(\neq i)} q_\alpha q_j \int d^3\mathbf{r}_1 \int d^3\mathbf{r}_2 \frac{f_\alpha(\mathbf{r}_1)f_j(\mathbf{r}_2)}{\mathbf{r}_{12}} \right\} \quad (24)
 \end{aligned}$$

as the electrostatic term, and

$$F^\alpha = E_0^\alpha A^\alpha \left[\left(\sum \rho^{\text{Al}} + \sum \rho^{\text{Fe}} + \sum \rho^{\text{O}} \right) \ln \left(\sum \rho^{\text{Al}} + \sum \rho^{\text{Fe}} + \sum \rho^{\text{O}} \right) \right]^{B^\alpha}, \quad (25)$$

as the cluster functional term, and

$$\begin{aligned}
 \phi_{pair}^\alpha = \frac{1}{2} \sum_{i, j(j \neq i)} \left\{ \sum_{\alpha, \beta} \psi_0^{\alpha-\beta} \{ \exp[-2\gamma^{\alpha-\beta}(r-t^{\alpha-\beta})] - 2 \exp[-\gamma^{\alpha-\beta}(r-t^{\alpha-\beta})] \} \right. \\
 - \sum_{\alpha, \beta} \psi_0^{\alpha-\beta} \{ \exp[-2\gamma^{\alpha-\beta}(D^{\alpha-\beta}-t^{\alpha-\beta})] - 2 \exp[-\gamma^{\alpha-\beta}(D^{\alpha-\beta}-t^{\alpha-\beta})] \} \\
 \left. - \sum_{\alpha, \beta} \frac{D^{\alpha-\beta}}{20} \left[1 - \left(\frac{r}{D^{\alpha-\beta}} \right)^{20} \right] \{ -2\gamma^{\alpha-\beta} \exp[-2\gamma^{\alpha-\beta}(D^{\alpha-\beta}-t^{\alpha-\beta})] + 2\gamma^{\alpha-\beta} \exp[-\gamma^{\alpha-\beta}(D^{\alpha-\beta}-t^{\alpha-\beta})] \} \right\}, \quad (\beta) = \{\text{Al, Fe, O}\} \quad (26)
 \end{aligned}$$

as the pair interaction term. In the Al phase of the composite, only F^{Al} and ϕ_{pair}^{Al} terms are used. In these terms, Al-O and Al-Fe interactions are not considered. The parameters in these terms are obtained by fitting to the properties of fcc Al. In the Fe_2O_3 phase of the composite, $E_{ES}^{\text{Fe}}, E_{ES}^{\text{O}}, F^{\text{Fe}}, F^{\text{O}}, \phi_{pair}^{\text{Fe}}$ and ϕ_{pair}^{O} terms are used. In these terms, Fe-Al and O-Al interactions are not considered. The parameters in these terms are obtained by fitting to the properties of $\alpha\text{-Fe}_2\text{O}_3$.

At the interfaces of Al and Fe_2O_3 , all the above terms with the inclusion of an additional term E_{ES}^{Al} are considered. E_{ES}^{Al} is used to account for the possibility that Al atoms at the interface may be oxidized under the effect of charged Fe and O atoms. Electronegativity equalization, cf. Strietz and Mintmire,⁷ is carried out to determine atomic charges of the Al, Fe, and O atoms in an interfacial region covered by the short range electrostatic cutoff radius (10 Å). The value of 10 Å here is obtained by matching the values of the Coulomb energy and the Coulomb virial as a function of the short range electrostatic cutoff. In addition, a convergence analysis for the variation in the electrostatic energy as a function of the short range cutoff is carried out. The value of 10 Å satisfied both criteria. This choice of cutoff radius corresponds to a description of the homogeneous crystalline systems. It is possible that nanocrystalline grain deformation mechanisms may be affected by changes in the cutoff radius, e.g., see Ogata *et al.*³² In this respect, the use of the interatomic potential in nanocrystalline structures involves a degree of approximation.

The electronegativity equalization is based on a description of the total electrostatic energy of an array of atoms as a function of the atomic charges (valences) and their positions, see Eqs. (9) and (19). For well-behaved parameters J_i^0 and functions $f_i(r)$, the electrostatic energy has a well-defined minimum. The values of charges q_i are chosen such that the

electrostatic energy E_{es} is minimized subject to the constraint that the sum of charges is constant, see Strietz and Mintmire.⁷ This condition is algebraically equivalent to the electronegativity equalization condition which requires that the chemical potentials $\mu = \mu_i = \partial E_{es} / \partial q_i$ be equal. With the consideration of all $E_{ES}^{\text{Al}}, E_{ES}^{\text{Fe}}, E_{ES}^{\text{O}}, F^{\text{Al}}, F^{\text{Fe}}, F^{\text{O}}, \phi_{pair}^{\text{Al}}, \phi_{pair}^{\text{Fe}}$ and ϕ_{pair}^{O} terms, the behavior of Al, Fe, and O atoms at Al- Fe_2O_3 interfaces can be accounted for. This procedure for calculating interatomic interactions in a composite represents an approximation and is one of the underlying assumptions of the MD framework in the current work. The potential is specific to Al-Al, Fe-Fe, Al-Fe, Al-O, Fe-O, and O-O interactions with parameters fitted to fcc Al, bcc Fe, $\alpha\text{-Al}_2\text{O}_3$, and $\alpha\text{-Fe}_2\text{O}_3$. The required fitting of all combinations of Al-Fe-O species to obtain bulk properties such as crystal lattice parameters, elastic constants, the surface energies and stacking fault energies of fcc Al, bcc Fe, $\alpha\text{-Al}_2\text{O}_3$, and $\alpha\text{-Fe}_2\text{O}_3$ represents a fairly large database. Therefore, the potential is regarded as reasonable for application to fcc Al+ $\alpha\text{-Fe}_2\text{O}_3$ composites. The accuracy for application to other polymorphs of alumina or of iron oxide is unknown, and, therefore, is not automatically recommended. Within this context, we surmise that the reasonable approximations of the Al-Al, Fe-Fe, Al-Fe, Al-O, Fe-O, and O-O interactions through fitting to the individual phase properties and consideration of the coupling of these interactions in the presence of each other using electronegativity equalization make it possible to describe interatomic interactions in a system that consists of a combination of the individual phases directly analyzed. A more accurate description of both composite structures and various polymorphs would involve more extensive fitting which perhaps can be the subject of a future paper. Such an endeavor can certainly benefit from more extensive *ab initio* calculations. Alternatively, it may be better pursued in a first principles setting.

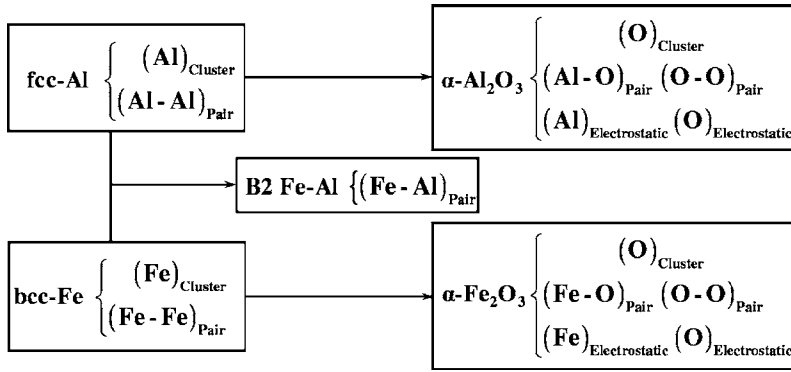


FIG. 1. Illustration of the fitting sequence.

III. FITTING AND TESTING OF THE POTENTIAL PARAMETERS

The potential parameters are determined by fitting the functional form to the lattice constants, cohesive energies, and elastic constants of fcc Al, bcc Fe, $\alpha\text{-Al}_2\text{O}_3$, and $\alpha\text{-Fe}_2\text{O}_3$. The parameters related to the Fe-Al pair interactions are determined by fitting to the formula unit energy of B2-FeAl. The fitting process involves the least square minimization of the sum of squared differences between target property values (experimental or *ab initio*) and values calculated from a trial parameter set. The minimization follows the genetic algorithm-based approach of Gale and Rohl³³ and is carried out for residual

$$F = \sum_k \omega_k [f_k - f_k(\mathbf{P}_{\text{trial}})]^2 \quad (27)$$

with respect to all possible choices of parameters. Here, ω_k are weights and are taken as unity and f_k represents the physical properties being fitted to. In this procedure, a functional parameter set corresponding to a global minimum of F is first obtained using a genetic algorithm, see Woodley *et al.*³⁴ and Cappello and Mancuso.³⁵ This parameter set is then subjected to refined local minimization using the Newton-Raphson (NR) approach. Use of the genetic algorithm before the NR scheme forms a general approach for the least square minimization of residual F , see Gale and Rohl.³³ An alternative is to use quantum mechanical treatments followed by an empirical fitting based on the physics of the problem, see Gale and Rohl.³³ Differences between the crystalline components and the lack of information regarding their interactions in the current work dictate the use of the genetic algorithm-based approach.

Since the potential is a combination of existing potentials for individual crystalline components in the literature, the initial trial parameter sets are taken to be those in the literature for the individual components. The NR fit starts with a numerical Hessian (second-order derivative matrix) and changes to Broyden-Fletcher-Goldfarb-Shanno (BFGS) updating of the exact Hessian (see Press *et al.*³⁶) based on the magnitude of the gradient norm of residual F as the gradient norm reduces in magnitude. Once the minimum of the gradient norm is obtained, the residual F is subjected to rational function optimization (RFO) (see Banerjee *et al.*³⁷) which removes imaginary modes from the Hessian, thus forcing it to be positive-definite and ensuring that the parameters ob-

tained correspond to a stable lattice structure. This structure in general is associated with nonzero internal forces at the atomic positions. Therefore, a relaxation fitting is carried out following the RFO step in order to zero out the internal forces. In this scheme, the displacements of the force-field optimized structure relative to the target structure also form part of the fitting function, as opposed to the use of only the forces on the atoms at the target structure as in a conventional fit, see Gale and Rohl.³³ This treatment is considered to be superior to conventional fitting schemes since it probes the forces as well as displacements, rather than just the former. During fitting, the density and functional parameters are obtained first, followed by the pair parameters and then the electrostatic parameters.

Figure 1 provides a schematic illustration of the fitting sequence. The Al and Fe cluster functional parameters and the Al-Al, Fe-Fe, and Al-Fe pair parameters are first determined by fitting to the properties of fcc Al, bcc Fe, and B2-FeAl. In subsequent fitting, the O cluster functional parameters, the O-O, Al-O, and Fe-O pair parameters, and the Al, Fe, and O electrostatic parameters are determined solely by fitting to the properties of $\alpha\text{-Al}_2\text{O}_3$ and $\alpha\text{-Fe}_2\text{O}_3$. During this procedure, the Al and Fe cluster functional parameters and the Al-Al and Fe-Fe pair parameters are kept constant. The Al electrostatic parameters and the Al-O pair parameters are solely determined by fitting to the properties of $\alpha\text{-Al}_2\text{O}_3$. The Fe electrostatic parameters and the Fe-O pair parameters are solely determined by fitting to the properties of $\alpha\text{-Fe}_2\text{O}_3$. However, the O cluster functional parameters, the O electrostatic parameters, and the O-O pair parameters are determined to obtain the best fit to the $\alpha\text{-Al}_2\text{O}_3$ and $\alpha\text{-Fe}_2\text{O}_3$ properties simultaneously. For this purpose, the Al and Fe electrostatic parameters and the Al-O and Fe-O pair parameters are determined first by fitting to the properties of $\alpha\text{-Al}_2\text{O}_3$ and $\alpha\text{-Fe}_2\text{O}_3$. Afterward, the fitting procedure focuses on varying the O cluster functional parameters, the O electrostatic parameters, and the O-O pair parameters while all other parameters are kept fixed. The fitting is carried out in a molecular statics code “*general utility lattice statics-1.3*” (GULP), by Gale and Rohl.³³ For the purpose of interatomic potential fitting, this code required implementation of the potential functional form. The specific information required is the functional form of the energy and its derivative up to the third order. GULP has the inherent ability to develop crystal structures from the specification of space group numbers (167 for Al_2O_3 and $\alpha\text{-Fe}_2\text{O}_3$, 224 for

TABLE I. Fitted and predicted properties of fcc Al. (*) indicates properties used for testing the fitted potential parameter set; (‡) indicates comparable polycrystalline values since single-crystalline values are unavailable.

		Mishin <i>et al.</i> ^a	Voter and Chen ^b	Experimental (<i>ab initio</i>)	Prediction
Lattice Properties	$a_0(\text{Å})$	4.05	4.05	4.05 ^c	4.05
	$E_0(\text{eV/atom})$	-3.36	-3.36	-3.36 ^c	-3.51
	$C_{11}(\text{GPa})$	114	107	114.3 ^d	116.56
	$C_{12}(\text{GPa})$	61.6	65.2	61.9 ^d	60.13
	$C_{44}(\text{GPa})$	31.6	32.2	31.6 ^d	25.13
	$B(\text{GPa})$	79	79	79 ^d	78.9
*Surface Energy	$\gamma_S(110)$ (mJ/m ²)	1006	959	980 ^{‡e}	1102.4
	$\gamma_S(111)$ (mJ/m ²)	870	823	980 ^{‡e}	913.7
	$\gamma_S(100)$ (mJ/m ²)	943	855	980 ^{‡e}	1001.5
*Stacking Fault Energy	γ_{SF} (mJ/m ²) $\frac{a}{6}\langle\bar{1}1\bar{2}\rangle\{111\}$	168/146	93/76	213(unstable), 166 (stable) ^{e,f}	265/175

^aReference 13.

^bReference 12.

^cWeast (Ref. 41).

^dSimons and Wang (Ref. 42).

^eMurr (Ref. 43).

^fHartford *et al.* (Ref. 44).

bcc Fe, and 229 for fcc Al). Once the functional form of the energy and its derivatives up to third order are implemented, the fitting is straightforwardly carried out using the procedure outlined.

Calculations of the elastic constants are based on the work of Catlow and Mackrodt³⁸ who use the Born and Huang³⁹ theory of crystal lattice. Their main contribution is the inclusion of crystal symmetry to speed up calculations. Temperature is not explicitly considered in this formulation. Instead,

the fitting is assumed to be carried out at the temperature at which the properties are specified. We use properties specified at 300 K. Table I–V show the properties of fcc Al, bcc Fe, $\alpha\text{-Al}_2\text{O}_3$, and $\alpha\text{-Fe}_2\text{O}_3$ used during fitting. The tables also show values of the lattice constants, elastic constants, and cohesive energies predicted by the potential. Reasonable agreement is seen between the predicted values and the experimental (*ab initio*) values. In the case of fcc Al, the fitting fares better than was the case for the potential of Voter and

TABLE II. Fitted and predicted properties of bcc Fe. (*) indicates properties used for testing the fitted potential parameter set; (‡) indicates comparable polycrystalline values since single-crystalline values are unavailable.

		Farkas <i>et al.</i> ^a	Experimental (<i>ab initio</i>)	Prediction
Lattice Properties	$a_0(\text{Å})$	2.87	2.87 ^b	2.87
	$E_0(\text{eV/atom})$	-4.28	-4.28 ^b	-4.28
	$C_{11}(\text{GPa})$	256	252 ^c	251.4
	$C_{12}(\text{GPa})$	136	138 ^c	136.7
	$C_{44}(\text{GPa})$	113	122 ^c	122
	$B(\text{GPa})$	173	173 ^c	174.93
*Surfaces Energy	$\gamma_S(110)$ (mJ/m ²)	1530	2100 ^{‡d}	1760
	$\gamma_S(111)$ (mJ/m ²)	2027	2100 ^{‡d}	2035.7
	$\gamma_S(100)$ (mJ/m ²)	1890	2100 ^{‡d}	1936.6
	γ_{US} (mJ/m ²)			
*Stacking Fault Energy	$\frac{a}{2}\langle 111\rangle\{110\}$	1100	...	1600/575

^aReference 17.

^bKittel (Ref. 45).

^cHirth and Lothe (Ref. 46).

^dMendelev *et al.* (Ref. 47).

TABLE III. Fitted and predicted properties of B2-FeAl.

		Experimental (<i>ab initio</i>)	Prediction
Lattice Properties	$a_0(\text{\AA})$	2.90 ^a	2.90
B2-FeAl	$E_0(\text{eV}/\text{Fe-Al pair})$	-8.15 ^b	-8.15

^aFu and Yoo (Ref. 48).^bHultgreen *et al.* (Ref. 49).

Chen.¹² In the case of bcc Fe, the fitting is comparable to the predictions made by the potential of Farkas *et al.*¹⁷ In the case of $\alpha\text{-Al}_2\text{O}_3$, the fitted properties compare well with the values provided by Strietz and Mintmire.⁷ For $\alpha\text{-Fe}_2\text{O}_3$, no comparable interatomic potential is available. Accordingly, the properties are compared to the experimental values provided by Huntington.⁴⁰ Overall, the predictions compare well with established potentials for the individual crystalline components.

Deformation analyses of a nanocrystalline system (single-phase or multiple-phase) require that interactions along interfaces as well as formations of line defects such as dislocations and planar defects (e.g., stacking faults) are well characterized by the interatomic potential, e.g., Kadau *et al.*,⁵⁵ Abraham,⁵⁶ Van Swygenhoven *et al.*,⁵⁷ and Buehler *et al.*¹ The potential already provides an accurate account for bulk modulus, elastic constants, lattice constants, and cohesive energies of the modeled crystal systems. We further require the potential to be able to predict the values of stacking fault and surface energies of the modeled crystal systems and compare well with those predicted by available potentials in literature. Based on the results from MD simulations of quasistatic deformation in nanocrystalline materials, e.g., Schiøtz and Jacobsen,⁵⁸ Van Swygenhoven *et al.*,⁵⁷ and of shock-induced deformation in single crystals, e.g., Kum⁵⁹

and Bringa *et al.*,⁶⁰ we surmise that the property database used for fitting and testing the parameters of the interatomic potential is sufficient to obtain a realistic description of deformation in the Al+Fe₂O₃ material system.

Table I–V show a comparison of the surface and generalized stacking fault energies of the crystalline components predicted by the potential with the corresponding experimental (*ab initio*) values reported in the literature. The calculations for fcc Al and bcc Fe use the approach of Zimmerman *et al.*⁶¹ In this approach, a shear displacement is given to one-half of a block of a single crystal relative to the other part. After the shear displacement, the energy per unit area of the crystalline block is calculated. The difference between this energy and the bulk energy per unit area is then plotted as a function of the shear displacement. As the shear displacement increases, the difference between the two energy values reaches a peak and then starts to dip. Later, it reaches a minimum at the shear displacement corresponding to the formation of a stable stacking fault. The peak of the curve is referred to as the unstable stacking fault energy (γ_{US} in Fig. 2) and the minimum is referred to as the stable stacking fault energy (γ_{SF} in Fig. 2). In Al, an $a/2\langle\bar{1}10\rangle$ unit dislocation dissociates into an $a/6\langle\bar{1}\bar{1}\bar{2}\rangle$ and an $a/6\langle\bar{1}2\bar{1}\rangle$ partial dislocation. Therefore, the energy associated with an $a/6\langle 112\rangle \times \{111\}$ partial dislocation is of importance. In Fe, the

TABLE IV. Fitted and predicted properties of $\alpha\text{-Al}_2\text{O}_3$. (*) indicates properties used for testing the fitted potential parameter set.

		Strietz and Mintmire ^a	Experimental (<i>ab initio</i>)	Prediction
Lattice Properties	Lattice Energy (eV)	-31.8	-31.8 (1 unit) ^b	-31.8
	$q_{\text{Al}}(\text{e})$	2.9	1.3 ^c	3.0
	$C_{11}(\text{GPa})$	537	497 ^d	505.9
	$C_{12}(\text{GPa})$	180	164 ^d	188.2
	$C_{13}(\text{GPa})$	106	111 ^d	97.77
	$C_{33}(\text{GPa})$	509	498 ^d	469.23
	$C_{14}(\text{GPa})$	-30	-24 ^d	-64.98
	$C_{44}(\text{GPa})$	130	147 ^d	165.97
	$a_0(\text{\AA})$	4.7602	4.7602 ^b	4.7602
	$C_0(\text{\AA})$	12.9912	12.9912 ^d	12.9912
* Surface Energy (mJ/m ²)	(0001) (unrelaxed)	3670	3770 ^e	3550
	(0001) (relaxed)	2670	1760 ^e	2500

^aReference 7.^bWeast (Ref. 41).^cLewis and Catlow (Ref. 50).^dWachtman Jr. *et al.* (Ref. 51).^eManassis and Gillan (Ref. 52).

TABLE V. Fitted and predicted properties of α -Fe₂O₃. (*) indicates properties used for testing the fitted potential parameter set.

Lattice Properties	Lattice Energy	Experimental (<i>abinitio</i>)	Prediction
	Lattice Energy (eV)	-101.178 (1 unit) ^a	-101.185
	$q_{Al}(e)$	2.602 ^a	3.0
	$C_{11}(\text{GPa})$	242 ^b	238.2
	$C_{12}(\text{GPa})$	55 ^b	50.72
	$C_{13}(\text{GPa})$	16 ^b	28.75
	$C_{33}(\text{GPa})$	228 ^b	223.08
	$C_{14}(\text{GPa})$	-13 ^b	-13.12
	$C_{44}(\text{GPa})$	85 ^b	78.05
	$a_0(\text{\AA})$	5.035 ^a	5.035
	$C_0(\text{\AA})$	13.747 ^a	13.747
*Surface Energy (mJ/m ²)	(0001) (unrelaxed)	5260 ^c	5540
	(0001) (relaxed)	1530 ^c	2050

^aCatti *et al.* (Ref. 53).

^bHuntington (Ref. 40).

^cMackrodt *et al.* (Ref. 54).

$a/2\langle 111 \rangle \{ 110 \}$ dislocation energy is of importance, cf. Farkas *et al.*¹⁷ To calculate the $a/6\langle 112 \rangle \{ 111 \}$ generalized stacking fault energy of Al, displacement increments of 0.25 Å are introduced on the $(1\bar{1}\bar{1})$ plane in the $\langle \bar{1}\bar{1}\bar{2} \rangle$ direction. The x , y , and z axes of the crystalline block are therefore aligned in the $\langle 11\bar{1} \rangle$, $\langle \bar{1}\bar{1}\bar{2} \rangle$, and $\langle \bar{1}10 \rangle$ crystallographic orientations, respectively. In Fe, the $a/2\langle 111 \rangle \{ 110 \}$ generalized stacking fault energy is calculated with displacement increments of 0.4 Å in the $\langle 111 \rangle$ direction on the (110) plane. The x , y , and z axes of the crystalline block are aligned in the $\langle 110 \rangle$, $\langle \bar{1}\bar{1}\bar{2} \rangle$, and $\langle 1\bar{1}\bar{1} \rangle$ crystallographic orientations, respectively. The energy vs shear displacement curves for the above calculations are shown in Fig. 2.

The potential overpredicts the stable and unstable stacking fault energies for both fcc Al and bcc Fe. In fcc Al, the extent of overprediction is the same as that of the well-established Mishin and Farkas potential, see Mishin *et al.*¹³ which has been extremely useful in modeling surface defect

formation in Al single crystals and polycrystals. For Fe, experimental or quantum mechanical values of the stacking fault energy are not available in the literature. Therefore, we choose to compare the results of our calculations with the results of a well-established Farkas *et al.*¹⁷ potential. The predicted value here is of the same order of magnitude as that given by the Farkas *et al.*¹⁷ potential. Overall, the stacking fault energies suggest that the potential compares well with existing single-component potentials in the literature when it is specialized to Al and Fe.

The thermodynamic penalty for cleaving a surface from a bulk material is measured by the surface energy. Given a bulk energy of E_{bulk} and an energy E_{surf} for the same system with a surface created, the surface energy is defined as $\gamma_s = (E_{bulk} - E_{surf})/A$. Here, A is the area of the newly created surface, cf. Gale and Rohl.³³ In this paper, we follow the approach of Strietz and Mintmire⁷ for calculating γ_s by creating a free surface along the desired cleavage direction using three-dimensional (3D) periodic boundary conditions (PBCs), see Gale and Rohl.³³ The unrelaxed surface energy is calculated by subtracting the energy of bulk crystal from the energy of an unrelaxed cleaved crystal. The relaxed surface energy is calculated by subtracting the energy of bulk crystal from the energy of a relaxed cleaved crystal (via MD equilibration at near 0 K). Since the surface energy values reported in the literature for fcc Al and bcc Fe are not highly reliable, it is desired that the surface energies of low-index planes such as $\{100\}$, $\{110\}$, and $\{111\}$ planes be close to the surface energy of an average orientation. This value is 980 mJ/m² for fcc Al (Mishin *et al.*¹³) and 2452 mJ/m² for bcc Fe (Murr⁴³). In addition, we require that $\gamma_s\{110\} > \gamma_s\{100\} > \gamma_s\{111\}$ in fcc Al and $\gamma_s\{111\} > \gamma_s\{100\} > \gamma_s\{110\}$ in bcc Fe. Both of these requirements are met, as shown in Tables I and II. For α -Fe₂O₃ and α -Al₂O₃, the surface energy values for $\{0001\}$ surface are calculated. Both the relaxed and unrelaxed values are quite close to what is reported in the literature, see Mackrodt *et al.*⁵⁴ and Manassis and Gillan,⁵² see Tables IV and V.

Overall, the potential along with the parameter set in Tables VI and VII offers a useful tool for analyzing deformation in the fcc Al + α -Fe₂O₃ material system. The potential is implemented in the scalable parallel MD code DL-POLY 2.14, see Smith *et al.*,⁶² which uses the atom-decomposition paradigm, see Vincent and Merz.⁶³ The next sections discuss the results of analyses on the mechanical deformation of a nanocrystalline Al + Fe₂O₃ system using the potential.

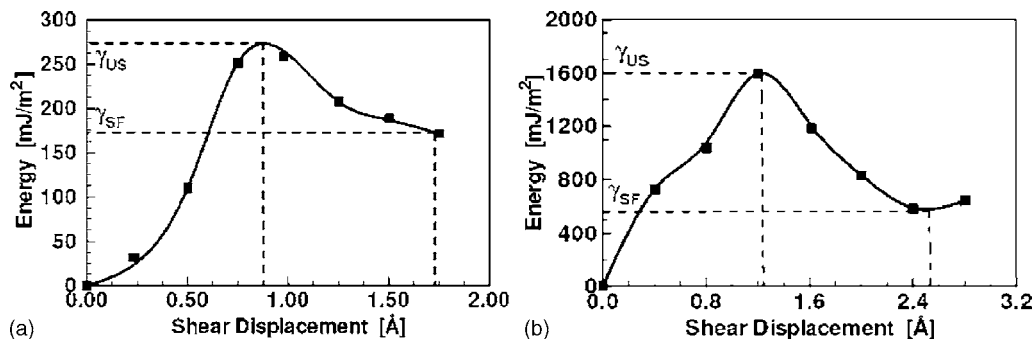

 FIG. 2. (a) Generalized $a/6\langle \bar{1}\bar{1}\bar{2} \rangle \{ 111 \}$ stacking fault energy of fcc Al; (b) generalized $a/2\langle 111 \rangle \{ 110 \}$ stacking fault energy of bcc Fe.

TABLE VI. Pair parameters of the potential.

	Ψ (eV)	t (Å)	γ (Å ⁻¹)	Cutoff (Å)
Al-Al	237.008963	4.003143	0.006436	7.0
Al-O	39.770657	1.021318	1.160757	7.0
Al-Fe	79.232208	2.098726	0.946525	7.0
Fe-Fe	1.073706	2.58029	0.969895	7.0
O-O	10.180285	1.0000	0.763738	7.0
Fe-O	2.653694	0.999972	2.110824	7.0

IV. GENERATION OF NANOCRYSTALLINE STRUCTURES

Nanocrystalline structures generated for deformation analyses are:

(1) Nanocrystalline Al with three different average grain sizes (PA11 with an average grain size of 7.2 nm, PA12 with an average grain size of 4.7 nm, and PA13 with an average grain size of 3.9 nm);

(2) Nanocrystalline α -Fe₂O₃ with three different average grain sizes (PHt1 with an average grain size of 7.2 nm, PHt2 with an average grain size of 4.7 nm, and PHt3 with an average grain size of 3.9 nm); and

(3) Nanocrystalline Al+ α -Fe₂O₃ composites with two different volume fractions: (a). 60% fcc Al+40% α -Fe₂O₃ (NCP641 with an average grain size of 7.2 nm, NCP642 with an average grain size of 4.7 nm, and NCP643 with an average grain size of 3.9 nm), (b). 40% fcc Al+60% α -Fe₂O₃ (NCP461 with an average grain size of 7.2 nm, NCP462 with an average grain size of 4.7 nm, and NCP463 with an average grain size of 3.9 nm).

Nanocrystalline Al, α -Fe₂O₃, and their composites with the same average grain size have the same grain orientation and grain size distributions. The structures are generated by growing grains inside a cubic box.

Grain orientations in the nanocrystalline structures play an important role in determining structural strength. Schiøtz *et al.*⁶⁴ have previously carried out such an analysis and found that the difference in strengths at various volume fractions is of the order of 5%. This difference increases as the number of grains decreases. However, it does not exceed 10% of the mean value. Since the purpose of the current work is to verify the strength predictions made using the potential developed here and to analyze the dependence of strength on the volume fractions, we have considered only one particular mix of orientations. In order to simulate bulk nanocrystalline materials, the box is repeated in all three dimensions by imposing periodic boundary conditions (PBCs). Imposition of PBCs results in a nanocrystalline structure that

has unimodal distribution of grain sizes. Size of the cubic box is limited by the maximum number of atoms that can be accommodated in the nanocrystalline structure confined in the box. The maximum number of atoms is limited by factors such as the memory and the CPU time required for carrying out MD simulations at a time scale of the order of picoseconds for a given interatomic potential. Taking into account these considerations, the size of the cubic box is kept at 10 nm × 10 nm × 10 nm such that the maximum number of atoms does not exceed 100 000. With this limitation, the largest grain size obtained by the bidivision of the cubic box in all three dimensions (a total of 8 grains) is approximately 8.2 nm with the average grain size being 7.2 nm.

Approaches frequently used for generating nanocrystalline structures are the monodisperse grain growth method; see Gleiter,⁶⁵ the melt growth method, see Kebabinski *et al.*;⁶⁶ and the Voronoi tessellation method, see Voronoi,⁶⁷ Chen,⁶⁸ and Schiøtz *et al.*⁶⁴ The monodisperse grain growth technique is nonstatistical in nature. The Voronoi tessellation method follows a fixed Voronoi-Poisson grain-size distribution which is rarely observed in experiments, see Gross and Li.⁶⁹ However, mesoscale simulations show that a Voronoi starting structure evolves very quickly toward (but never reaches) a log-normal distribution, see Haslam *et al.*⁷⁰ Gross and Li⁶⁹ have combined the Monte Carlo method with the Voronoi tessellation method for grain growth to generate nanocrystalline structures with specified distribution of grain size. This procedure is also similar to that of Chen.⁶⁸ We follow a similar procedure here. We generated nanocrystalline structures with three different average grain sizes: (1) structures with 8 grains and an average grain size of 7.2 nm; (2) structures with 27 grains and an average grain size of 4.7 nm; and (3) structures with 64 grains and an average grain size of 3.9 nm. All nanocrystalline structures follow log-normal grain-size distribution with 10% standard deviation. Figure 3 shows the nanocrystalline structures with different average grain sizes and volume fractions of the Al phase.

After geometric generation, all structures are equilibrated at 300 K with PBCs applied in all directions. In Fig. 4, the partial Al-Al radial distribution functions (RDFs) before and after the MD equilibration for all nanocrystalline Al structures are shown. The RDFs differ from that of a perfect fcc-Al crystal before and after equilibration in two ways. First, the peaks are not sharp delta functions and are somewhat smeared even before equilibration due to a degree of mismatch along the grain boundaries. Second, the RDFs do not approach zero after the first two peaks. The broadening of the RDF peaks after equilibration is in part due to the strain fields inside the grains (originating from the grain

TABLE VII. Cluster and electrostatic parameters of the potential.

	A	B	E_0 (eV)	r_0 (Å)	β_0 (Å ⁻¹)	t_0	χ (eV)	J (eV)	ξ (Å ⁻¹)	Z
Al	0.9739	1.000	4.769	-3.024332	0.938493	86.15	-55.333	1.94422	0.77344	3.5245
Fe	0.041333	1.000	7.659	1.743248	1.01471	2.128185	1.5834	2.59674	0.595758	6.2
O	1.000	1.000	2.558	1.412648	1.806365	0.895404	5.48	14.03	2.14	0.0

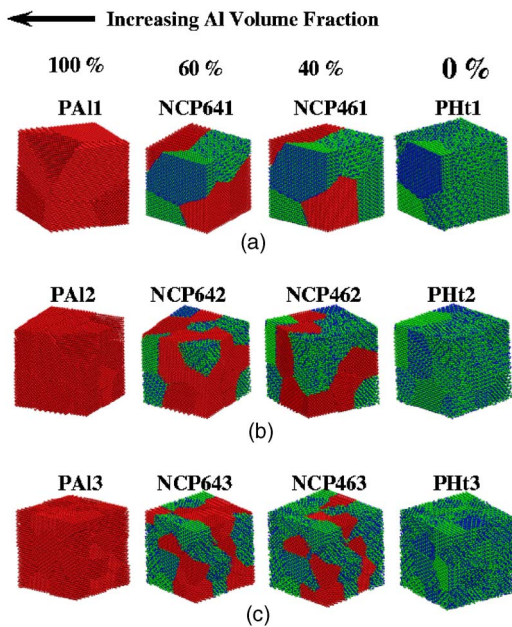


FIG. 3. (Color online) Nanocrystalline structures with different Al volume fractions and grain sizes; (a) 7.2 nm, (b) 4.7 nm, and (c) 3.9 nm (Al atoms are red, Fe atoms are blue, and O atoms are green).

boundaries) and in part due to atoms in or near the grain boundaries sitting close to (but not at) the lattice positions. The fact that the RDF does not go to zero between the peaks denotes a disorder which in this case comes from the grain boundaries. The average depth of the RDF valleys decreases with the average grain size. Clearly, this is due to the fact that at small grain sizes the fraction of atoms in grain boundaries is higher. PA11 has a higher fraction of atoms in bulk fcc-Al crystalline order and therefore sharper RDF peaks than PA12 and PA13. Similar features are observed for all structures as well. MD simulations are performed in uniaxial tension and compression using the method of Schiøtz *et al.*⁶⁴ and Schiøtz *et al.*⁷¹ In this method, an algorithm based on a combination of NPT and NVT ensembles is used. Quasistatic deformation is carried out by stretching samples in one direction. Stretching at a specified rate is carried out using a modified version of the Melchionna *et al.*⁷² NPT equations of motion, cf. Spearot *et al.*⁷³ The strain is calculated by recording the position of individual atoms. The average stress is

evaluated at each strain level to yield stress-strain relations. An alternative is to use the method of Van Swygenhoven and Caro⁷⁴ who recorded strain-time curves at different values of applied stress. Spearot *et al.*⁷³ have used both methods and found that the modified Schiøtz *et al.*⁶⁴ works better by simulating a controlled displacement test.

V. TENSILE DEFORMATION OF POLYCRYSTALLINE Al

The simulations focus on analyzing the accuracy of the interatomic potential. Consequently, calculated strength values are compared with the experimental measurements. In addition, defect attributes are also analyzed using the potential. In the following discussions, the flow strength is calculated as the average stress in the region on the stress-strain curve where stress reaches its maximum. This procedure is similar to that of Schiøtz *et al.*⁶⁴ and is chosen for facilitating comparisons. Extensive experimental as well as theoretical research has been carried out to analyze the deformation mechanisms in nanocrystalline Al and other fcc materials, e.g., Lu *et al.*⁷⁵ Chung *et al.*⁷⁶ Dalla Torre and Van Swygenhoven,⁷⁷ Yamakov *et al.*,⁷⁸ Chen *et al.*,⁷⁹ and Liao *et al.*⁸⁰ Most MD simulations have been performed on fully dense metals (primarily Ni, Cu, and Pd). The samples are free of impurities with adjacent grains separated primarily by high-angle grain boundaries. MD simulations have established that the deformation mechanisms at room temperature fall into three main categories. These are

- (1) Intergranular mechanisms consisting of uncorrelated atom shuffling at high-angle grain boundaries which results in grain boundary sliding, cf. Schiøtz *et al.*⁷¹ and Schiøtz *et al.*,⁶⁴
 - (2) Intragranular mechanisms such as partial dislocation emission and twinning in nanocrystalline metals with grain sizes larger than 10 nm, cf. Liao *et al.*,⁸¹ and
 - (3) Cooperative grain behaviors, i.e., microshear banding or rotation of clusters of grains, cf. Hasnaoui *et al.*⁸²
- A combination of the above deformation mechanisms is observed during MD simulations here. Figure 5(a) shows the stress-strain curves for PA11, PA12, and PA13 in tension. The values of Young’s modulus are 57.7 GPa for PA11, 33.9 GPa for PA12, and 48.4 GPa for PA13. The flow stress is taken as the average of the stress values at strain levels of 4%, 6%, and 8%. These strain levels are chosen because the stress in at least one of the structures either becomes constant or

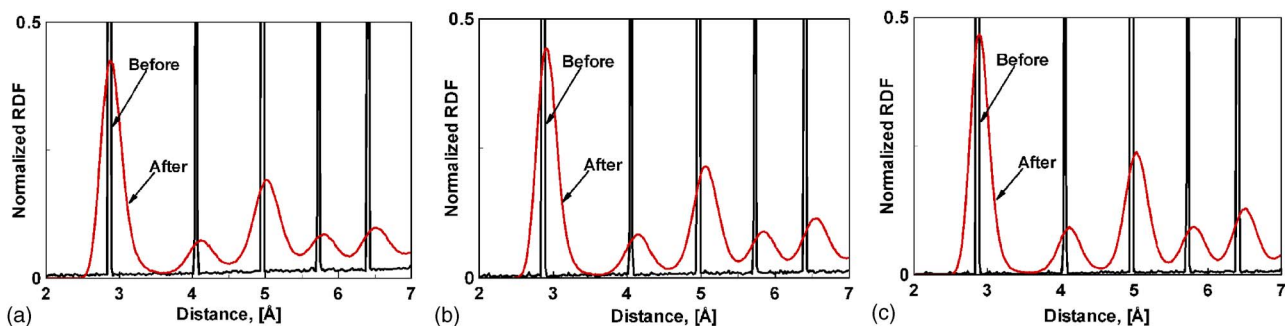


FIG. 4. (Color online) A comparison of the partial Al-Al RDFs for nanocrystalline Al with grain size of (a) 3.9 nm, (b) 4.7 nm, and (c) 7.2 nm, before and after MD equilibration.

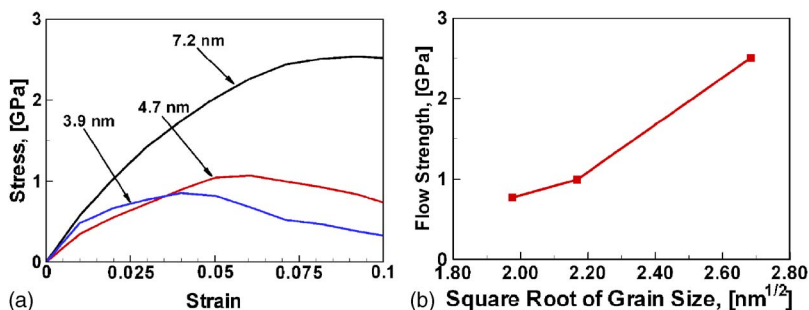


FIG. 5. (Color online) (a) Tensile stress-strain curves for nanocrystalline Al with different grain sizes and (b) dependence of flow strength on average grain size for nanocrystalline Al.

reaches a maximum at one of these strain values. We note that similar strain levels have been used by other researchers, e.g., Schiøtz *et al.*⁶⁴ and Lu *et al.*⁷⁵ The flow strength is found to be 2.5 GPa for PA11, 0.98 GPa for PAI2, and 0.74 GPa for PAI3. Overall, a softening trend in strength is observed as the average grain size decreases. One exception exists in the Young's modulus value of PAI3 which is higher than that of PAI2. Similar anomalies in stress-strain relations have been observed in the work of Schiøtz and Jacobsen⁵⁸ on nanocrystalline Cu. This behavior can be explained by accounting for the role of grain boundaries in the deformation. At the length scale of analyses, sliding of grains along grain boundaries is the primary mechanism of deformation. Dislocation activity is minimal at this length scale. Total grain boundary surface area increases as the grain size decreases, resulting in softening of the structures. When the size scales are similar for two structures, the difference in the fractions of grain boundaries with high-angle mismatch and the difference in the fractions of atoms in defects and grain boundaries play an important role. Higher fractions of defect atoms and high-angle mismatch grain boundaries in PAI3 as compared to those in PAI2 pose enhanced constraint on the movement of atoms in PAI3 during initial stretching. The atoms locked in the high-angle grain boundaries resist initial tensile deformation, making PAI3 initially stronger than PAI2. However, after significant deformation, the flow is mainly governed by grain boundary sliding which is dominant in PAI3. Because of the increased elongation, grain boundary atoms have stronger mobility in PAI3 than in PAI2 during later stages of deformation. Accordingly, PAI3 has a lower flow strength value than PAI2.

The Young's modulus for these structures varies from 33.9 GPa to 57.7 GPa and increases with grain size. These values are smaller than the value of 70 GPa for single-crystalline Al. Similarly, values ranging from 90–105 GPa

are seen in nanocrystalline Cu, compared with the value of 124 GPa for bulk Cu, cf. Gschneidner.⁸³ As explained earlier, the primary reason behind this trend is that the atoms in grain boundaries cause the Young's modulus to decrease. A similar observation is made in simulations where the nanocrystalline metal is grown from a molten phase, see Phillpot *et al.*⁸⁴ In our research, plastic yielding occurs at stress values of approximately 0.5–1.5 GPa in the structures analyzed. It is illustrative to note that, the theoretical shear strength of single crystalline Al ($Gb/2\pi d$) is approximately 3 GPa.

Figure 5(b) shows the variations of the flow strengths with square root of the average grain size. Overall, a reverse Hall-Petch (H-P) relation is observed. A similar effect has been observed by Schiøtz *et al.*⁷¹ and Schiøtz *et al.*⁶⁴ in defect free nanocrystalline Cu and by Latapie and Farkas⁸⁵ in nanocrystalline α -iron. These are consistent with the experimental data of Bonetti *et al.*⁸⁶ At smaller grain sizes, the arrangement of low-angle and high-angle grain boundaries plays an important role in deformation. Consequently, the dependence of flow strength on the square root of the average grain sizes deviates from a linear trend. A similar observation is reported by Schiøtz *et al.*⁷¹ for nanocrystalline Cu, by Liao *et al.*⁸⁰ for nanocrystalline Ni, and by El-Sherik *et al.*⁸⁷ in experiments on electroplated nanocrystalline Ni.

Grains in all nanocrystalline structures have three primary orientations, viz. [100], [110], and [111]. Adjacent grains are randomly rotated relative to each other. In the case of PAI, this procedure results in a random placement of the low-angle mismatch and high-angle mismatch grain boundaries. One such cross section of PAI1 is shown in Fig. 6(a). The {100}-{100} low-angle mismatch grain boundary is shown with a broken line. The {100}-{110}, {110}-{110}, {110}-{111}, and {111}-{100} high-angle mismatch grain boundaries are shown with solid lines. In order to compare deformation mechanisms in nanocrystalline Al with those reported in the

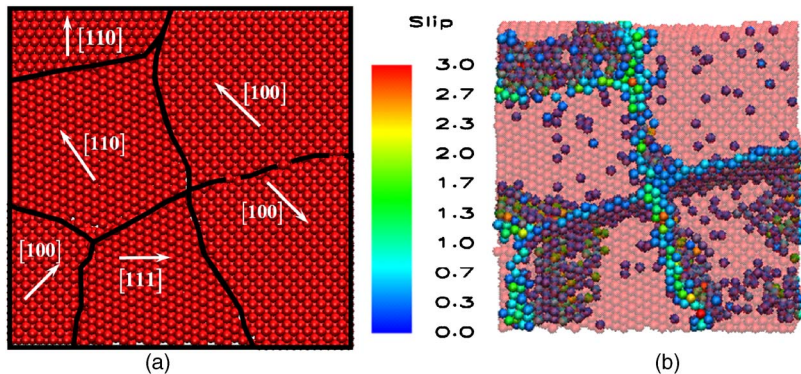


FIG. 6. (Color online) (a) Identification of grain boundary mismatch in nanocrystalline Al with grain size 7.2 nm and (b) identification of grain boundaries using the slip vector approach.

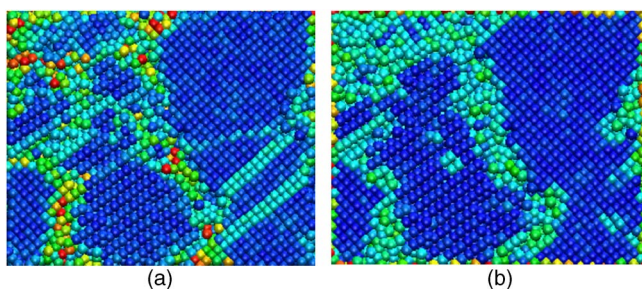


FIG. 7. (Color online) Defect formation in PA11 at a strain of 15% with atoms colored by (a) the slip-vector and (b) the centrosymmetry parameter approaches (red circles identify dislocations and old grain boundaries that disappear during deformation).

literature, two different visualization schemes are used. Specifically, the slip-vector approach by Zimmerman *et al.*⁸⁸ and the centrosymmetry parameter by Kelchner *et al.*⁸⁹ are used for identifying defect atoms in fcc Al. Figure 6(b) shows grain boundaries at the same cross section of PA11 with atoms colored using the slip-vector approach (the corresponding scale is also shown). In Al, the unit glissile dislocation is the $a/2[110]$ dislocation with a Burgers vector magnitude of 2.87 Å which is close to the upper limit of the slip-vector scale shown in Fig. 6(b). For clarity, the figure shows only those atoms that have slip-vector magnitudes above 0.25, eliminating the atoms that occupy bulk lattice positions. Clearly, atoms in grain boundaries can be easily differentiated from atoms inside the grains using the slip-vector approach. However, the slip-vector approach is not useful for identifying unit dislocations in structures made of, for example, fcc-Al lattices, e.g., cf. Van Swygenhoven *et al.*⁹⁰ Because of this, the centrosymmetry parameter by Kelchner *et al.*⁸⁹ is also used.

Recently, Van Swygenhoven *et al.*⁹⁰ found that partial dislocations are rarely observed in nanocrystalline Al because of the very small difference between the stable and unstable stacking fault energies of single-crystalline Al. Their simulations use Mishin and Farkas (Mishin *et al.*¹³) potential that is one of the most established potential for Al. In order to confirm that the potential developed here also shows this impor-

tant deformation feature, the defect formation in PA11 is analyzed. Figure 7(a) shows PA11 at 15% tensile strain with atoms colored using the slip-vector approach. For convenience of comparison, the same cross section as in Fig. 6(a) is shown. Clearly, the $\{100\}$ - $\{100\}$ low-angle mismatch grain boundaries are smeared out during the grain elongation associated with stretching. In addition, there is a dislocation emission from the $\{111\}$ - $\{100\}$ high-angle mismatch grain boundary. Figure 7(b) shows the same snapshot of the PA11 with atoms now colored using the centrosymmetry parameter approach. Consistent with the observations made parameter by Kelchner *et al.*⁸⁹ using the centrosymmetry, the $\{100\}$ - $\{100\}$ low-angle grain boundary is not visible in the figure. In addition, dislocations emitted from the $\{111\}$ - $\{100\}$ high angle mismatch grain boundary seen in Fig. 7(a) are also not seen here. From this observation, it can be concluded that unit dislocations are emitted in PA11. Similar observations are also recorded for PA12 and PA13. Obviously, the potential correctly predicts the formation of unit dislocations in nanocrystalline Al, see Van Swygenhoven *et al.*⁹⁰

VI. TENSILE DEFORMATION OF NANOCRYSTALLINE Al+Fe₂O₃ COMPOSITES

Figure 8 shows the Young’s moduli and the flow strengths in tension for all material samples analyzed as functions of the average grain size. In both Figs. 8(a) and 8(b), the H-P relationships show a clear dependence on the volume fractions of Al and Fe₂O₃. For the composite structures, the H-P relationships lie between those of PA1 and PHt. However, the relationships for the composites cannot be simply obtained from the relationships for PA1 and PHt based on the rule of mixture. This is primarily because the deformation in the composites is strongly affected by the Al-Fe₂O₃ interfaces. Depending on the relative orientations of the two phases at an interface, the contribution of the interface to the strength of a composite varies. Consequently, for larger average grain sizes the strength of the composites might be more accurately estimated based on the volume fractions of the individual phases. This is clear from the results for the 7.2 nm structures. Specifically, the strength for these structures can

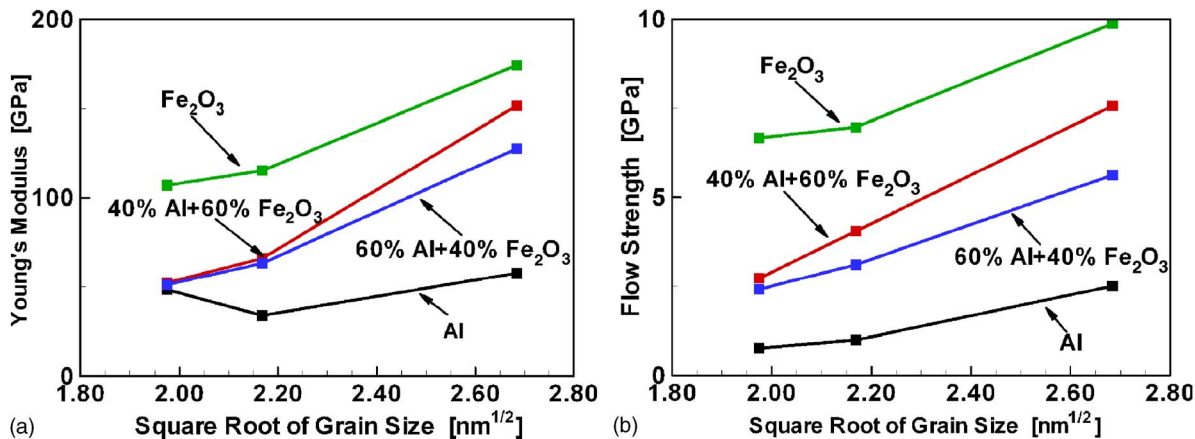


FIG. 8. (Color online) The dependence of (a) Young’s moduli and (b) flow strengths on grain size in all the nanocrystalline structures under tension.

be more closely obtained from those of the pure Al phase and pure Fe_2O_3 phase using the rule of mixture. This, however, cannot be carried out for the structures with average grain sizes of 4.7 nm and 3.9 nm. At these grain sizes, there is a nonproportional increase in the defect and interfacial atoms. Consequently, the interfacial and GB atoms have larger contributions to the calculated strength values. This result points out that it may be possible for nanocomposite structures to have a critical grain size above which the strength of a nanocomposite can be calculated using the rule of mixture. Below the critical grain size, the large volume of interfacial atoms in the composites causes the rule of mixture to be ineffective. The GB mismatch and the interfacial stresses also need to be considered to form an appropriate relation, especially at smaller grain sizes. The effects of GBs and interfaces diminish as the average grain size increases. For nanocrystalline structures with grain sizes in the domain where dislocations contribute significantly to the deformation mechanism, it should be possible to neglect the effects associated with GB mismatches and interfacial stresses.

Another important observation from Fig. 8 is that the strength-grain-size relations are strongly dependent on the volume fraction of Fe_2O_3 . Structures with higher volume fractions of Fe_2O_3 have steeper slopes in Fig. 8. This indicates that electrostatic forces enhance GB sliding in structures with smaller grain sizes. In both plots, the relationship between the strength and the square root of the grain size for nanocrystalline Al is not linear. This is because high-angle GBs play different roles in PAI2 and PAI3. The difference in the average grain sizes for PAI2 and PAI3 is very small. However, there is a big difference in the fraction of defect and GB atoms and in the arrangement of the low-angle and high-angle GBs. At the nanoscale grain sizes, interfaces and GBs dominate the deformation mechanism. Accordingly, the strength of a nanocrystalline structure is a function of the arrangement of GBs (low-angle vs high-angle) and interfaces in addition to the average grain size. Differences in the arrangement of GBs preclude a linear strength and the square root of average grain-size relationship. Similar trends in the H-P relationship are reported by Schiøtz *et al.*⁷¹ for nanocrystalline Cu, by Liao *et al.*⁸⁰ for nanocrystalline Ni, and by El-Sherik *et al.*⁸⁷ through experiments on electroplated Ni

samples. In all the cases, the Young's modulus values are lower than those found for the corresponding macrocrystalline values. The flow strength values for the pure phases approach the ideal shear strengths of the corresponding single-crystalline systems.

VII. SUMMARY

An interatomic potential for carrying out MD simulations of mechanical deformation in the fcc Al+ α - Fe_2O_3 material system is developed. This material system has a combination of metallic, covalent, and ionic bonds. Accordingly, the potential model includes an EAM functional, a Morse-type pair function, and a second-order electrostatic interaction functional. As far as we are aware, this potential is the first multicomponent interatomic potential for this system. The potential can be used in MD simulations of fcc Al, bcc Fe, α - Fe_2O_3 , and α - Al_2O_3 as well as for a system consisting of a combination of these crystalline components. The potential is fitted to the cohesive energy, the lattice constants, and the elastic constants of all the component systems. The potential predicts the surface and stacking fault energies of the component systems in good agreement with experimental measurements and first principles data. The predictions also compare well with the predictions of other established potentials in the literature. Application of the potential to the analyses of the deformation of nanocrystalline Al, nanocrystalline Fe_2O_3 , and their composites reveals that the potential can be used to obtain physical insights into the deformation of pure Al and pure Fe_2O_3 phases as well as into the mechanical deformation of Al+ Fe_2O_3 nanocomposites.

ACKNOWLEDGMENTS

Funding through a U.S. Air Force Office of Scientific Research MURI grant at Georgia Tech is acknowledged. Computations are carried out at ERDC, AHPCRC, ARL, and NAVO MSRCs. Authors thank Julian Gale for providing the molecular statics code GULP 1.3 and Will Smith for providing DL_POLY2.14 which are modified and used in the current research.

*Corresponding author. Email address: vikas.tomar@nd.edu

†Email address: min.zhou@me.gatech.edu

¹M. J. Buehler, A. Hartmaier, H. Gao, M. Duchaineau, and F. F. Abraham, *Comput. Methods Appl. Mech. Eng.* **193**, 5257 (2004).

²J. J. Granier and M. L. Pantoya, *Combust. Theory Modell.* **8**, 555 (2004).

³R. W. G. Wyckoff, *Crystal Structures* (John Wiley and Sons, New York, London, 1963).

⁴W. C. Mackrodt and R. F. Stewart, *J. Phys. C* **12**, 431 (1979).

⁵J. D. Gale, C. R. A. Catlow, and W. C. Mackrodt, *Modell. Simul. Mater. Sci. Eng.* **1**, 73 (1992).

⁶M. I. Baskes, *Phys. Rev. B* **46**, 2727 (1992).

⁷F. H. Streitz and J. W. Mintmire, *Phys. Rev. B* **50**, 11996 (1994).

⁸T. Ohira and Y. Inoue, in *MRS Symposia Proceedings No. 492* (Materials Research Society, Pittsburgh, 1998), p. 401.

⁹S. D. Kenny, D. Nguyen-Manh, H. Fujitani, and A. P. Sutton, *Philos. Mag. Lett.* **78**, 469 (1998).

¹⁰D. K. Belashchenko and O. I. Ostravski, *Thermochim. Acta* **372**, 143 (2001).

¹¹S. M. Foiles, M. I. Baskes, and M. S. Daw, *Phys. Rev. B* **33**, 7983 (1986).

¹²A. F. Voter and S. P. Chen, in *MRS Symposia Proceedings No. 82* (Materials Research Society, Pittsburgh, 1987), p. 175.

¹³Y. Mishin, D. Farkas, M. J. Mehl, and D. A. Papaconstantopoulos, *Phys. Rev. B* **59**, 3393 (1999).

- ¹⁴M. I. Baskes, M. Asta, and S. G. Srinivasan, *Philos. Mag. A* **81**, 991 (2001).
- ¹⁵R. Pasianot, D. Farkas, and E. J. Savino, *Phys. Rev. B* **43**, 6952 (1991).
- ¹⁶G. Simonelli, R. Pasianot, and E. J. Savino, in *MRS Symposia Proceedings No. 291* (Materials Research Society, Pittsburgh, 1993), p. 567.
- ¹⁷D. Farkas, M. J. Mehl, and D. A. Papaconstantopoulos, in *MRS Symposia Proceedings No. 653* (Materials Research Society, Pittsburgh, 2001), p. Z6.4.1.
- ¹⁸R. Besson and J. Morillo, *Phys. Rev. B* **55**, 193 (1997).
- ¹⁹C. Vailhe and D. Farkas, *Acta Mater.* **45**, 4463 (1997).
- ²⁰J. Tersoff, *Phys. Rev. B* **38**, 9902 (1988).
- ²¹D. W. Brenner, *Phys. Rev. B* **42**, 9458 (1990).
- ²²J. Che, T. Cagin, and W. A. Goddard III, *Theor. Chim. Acta* **102**, 346 (1999).
- ²³R. K. Kalia, T. J. Campbell, A. Chatterjee, A. Nakano, P. Vashishta, and S. Ogata, *Comput. Phys. Commun.* **128**, 245 (2000).
- ²⁴W. J. Mortier, K. V. Genechten, and J. Gasteiger, *J. Am. Chem. Soc.* **107**, 829 (1985).
- ²⁵A. K. Rappe and W. A. Goddard III, *J. Phys. Chem.* **95**, 3358 (1991).
- ²⁶S. W. Rick, S. J. Stuart, and B. J. Berne, *J. Chem. Phys.* **101**, 6141 (1994).
- ²⁷Y.-P. Liu, K. Kim, J. Berne, R. A. Friesner, and S. W. Rick, *J. Chem. Phys.* **108**, 4739 (1997).
- ²⁸W. A. Goddard III, Q. Zhang, M. Uludogan, A. Strachan, and T. Cagin, in *Fundamental Physics of Ferroelectrics*, edited by R. Cohen and T. Egami (American Institute of Physics, Washington, DC, 2002), Vol. 626, p. 45.
- ²⁹A. E. Carlsson, *Solid State Phys.* **43**, 1 (1990).
- ³⁰R. G. Parr and R. G. Pearson, *J. Am. Chem. Soc.* **105**, 7512 (1983).
- ³¹C. C. J. Roothan, *J. Chem. Phys.* **19**, 1445 (1951).
- ³²S. Ogata, H. Iyetomi, K. Tsuruta, F. Shimojo, A. Nakano, R. K. Kalia, and P. Vashishta, *J. Appl. Phys.* **88**, 6011 (2000).
- ³³J. D. Gale and A. L. Rohl, *Mol. Simul.* **29**, 291 (2003).
- ³⁴S. M. Woodley, P. D. Battle, J. D. Gale, and R. A. Catlow, *Phys. Chem. Chem. Phys.* **1**, 2535 (1999).
- ³⁵F. Cappello and A. Mancuso, *CAD* **35**, 761 (2003).
- ³⁶W. H. Press, S. A. Teukolsky, W. T. Vetterling, and B. P. Flannery, *Numerical Recipes* (Cambridge University Press, Cambridge, 1992).
- ³⁷A. Banerjee, N. Adams, J. Simons, and R. Shepard, *J. Phys. Chem.* **89**, 52 (1985).
- ³⁸C. R. A. Catlow and W. C. Mackrodt, in *Computer Simulation of Solids*, edited by H. Araki, J. Ehlers, K. Hepp, R. Kippenhahn, H. A. Weidenmuller, and J. Zittartz, *Lecture Notes in Physics* 166 (Springer-Verlag, Berlin, 1982).
- ³⁹M. Born and K. Huang, *Dynamical Theory of Crystal Lattices* (Clarendon Press, Oxford, 1954).
- ⁴⁰H. B. Huntington, in *Solid State Physics: Advances in Research and Applications*, edited by F. Seitz and D. Turnbull (Academic Press, New York, 1958), Vol. 7, p. 213.
- ⁴¹R. C. Weast, *Handbook of Chemistry and Physics* (CRC, Boca Raton, FL, 1984).
- ⁴²G. A. Simons and H.-T. Wang, *Single Crystal Elastic Constants and Calculated Aggregate Properties* (MIT-Press, Cambridge, MA, 1977).
- ⁴³L. E. Murr, *Interfacial Phenomenon in Metals and Alloys* (Addison-Wesley Publishing Company, Reading, MA, 1975).
- ⁴⁴J. Hartford, B. von Sydow, G. Wahnstrom, and B. I. Lundqvist, *Phys. Rev. B* **58**, 2487 (1998).
- ⁴⁵C. Kittel, *Introduction to Solid State Physics* (Wiley-Interscience, New York, 1986).
- ⁴⁶J. P. Hirth and J. Lothe, *Theory of Dislocations* (Krieger Publishing Company, Melbourne, FL, 1982).
- ⁴⁷M. I. Mendeleev, S. Han, and D. J. Srolovitz, *Philos. Mag.* **83**, 3977 (2003).
- ⁴⁸C. L. Fu and M. H. Yoo, *Acta Metall. Mater.* **40**, 703 (1992).
- ⁴⁹R. Hultgreen, P. D. Desai, D. T. Hawkins, M. Gleiser, and K. K. Kelley, *Selected Values of the Thermodynamic Properties of Binary Alloys* (American Society for Metals, Metals Park, OH, 1973).
- ⁵⁰G. V. Lewis and C. R. A. Catlow, *J. Phys. C* **18**, 1149 (1985).
- ⁵¹J. B. Wachtman Jr., W. E. Tefft, D. G. Lam Jr., and C. S. Apstein, *Phys. Rev.* **122**, 1754 (1961).
- ⁵²I. Manassidis and M. J. Gillan, *J. Am. Chem. Soc.* **77**, 335 (1994).
- ⁵³M. Catti, G. Valerio, and R. Dovesi, *Phys. Rev. B* **51**, 7441 (1995).
- ⁵⁴W. C. Mackrodt, R. J. Davey, and S. N. Black, *J. Cryst. Growth* **80**, 441 (1987).
- ⁵⁵K. Kadau, T. C. Germann, P. S. Lomdahl, and B. L. Holian, *Science* **296**, 1681 (2002).
- ⁵⁶F. F. Abraham, *Adv. Phys.* **52**, 727 (2003).
- ⁵⁷H. Van Swygenhoven, P. M. Derlet, and A. G. Froseth, *Nat. Mater.* **3**, 399 (2004).
- ⁵⁸J. Schiøtz and K. W. Jacobsen, *Science* **301**, 1357 (2003).
- ⁵⁹O. Kum, *J. Appl. Phys.* **93**, 3239 (2003).
- ⁶⁰E. M. Bringa, J. U. Cazamias, P. Erhart, J. Stoelken, N. Tanushev, B. D. Wirth, R. E. Rudd, and M. J. Caturla, *J. Appl. Phys.* **96**, 3793 (2004).
- ⁶¹J. A. Zimmerman, H. Gao, and F. F. Abraham, *Modell. Simul. Mater. Sci. Eng.* **8**, 103 (2000).
- ⁶²W. Smith, C. W. Yong, and P. M. Rodger, *Mol. Simul.* **28**, 385 (2002).
- ⁶³J. Vincent and K. M. Merz, *J. Comput. Chem.* **11**, 1420 (1995).
- ⁶⁴J. Schiøtz, T. Vegge, F. D. Di Tolla, and K. W. Jacobsen, *Phys. Rev. B* **60**, 11971 (1999).
- ⁶⁵H. Gleiter, *Acta Mater.* **48**, 1 (2000).
- ⁶⁶P. Keblinski, D. Wolf, and H. Gleiter, *Interface Sci.* **6**, 205 (1998).
- ⁶⁷G. F. Voronoi, *J. Reine Angew. Math.* **133**, 97 (1908).
- ⁶⁸D. Chen, *Comput. Mater. Sci.* **3**, 327 (1995).
- ⁶⁹D. Gross and M. Li, *Appl. Phys. Lett.* **80**, 746 (2002).
- ⁷⁰A. J. Haslam, S. R. Phillpot, D. Wolf, D. Moldovan, and H. Gleiter, *Mater. Sci. Eng., A* **318**, 293 (2001).
- ⁷¹J. Schiøtz, F. D. Di Tolla, and K. W. Jacobsen, *Nature (London)* **391**, 561 (1998).
- ⁷²S. Melchionna, G. Ciccotti, and B. L. Holian, *Mol. Phys.* **78**, 533 (1993).
- ⁷³D. E. Spearot, K. I. Jacob, and D. L. McDowell, *Acta Materialia* (to be published).
- ⁷⁴H. Van Swygenhoven and A. Caro, *Appl. Phys. Lett.* **71**, 1652 (1997).
- ⁷⁵L. Lu, S. X. Li, and K. Lu, *Scr. Mater.* **45**, 1163 (2001).
- ⁷⁶C. S. Chung, J. Kim, H. Kim, and W. Kim, *Mater. Sci. Eng., A* **337**, 39 (2002).
- ⁷⁷F. Dalla Torre and H. Van Swygenhoven, *Acta Mater.* **50**, 3957

- (2002).
- ⁷⁸V. Yamakov, D. Wolf, S. R. Phillpot, and H. Gleiter, *Acta Mater.* **50**, 5005 (2002).
- ⁷⁹M. Chen, E. Ma, K. J. Hemker, Y. M. Wang, and X. Cheng, *Science* **300**, 1275 (2003).
- ⁸⁰X. Z. Liao, S. G. Srinivasan, Y. H. Zhao, M. I. Baskes, Y. T. Zhua, F. Zhou, E. J. Lavernia, and H. F. Xu, *Appl. Phys. Lett.* **84**, 3564 (2004).
- ⁸¹X. Z. Liao, F. Zhou, E. J. Lavernia, S. G. Srinivasan, M. I. Baskes, D. W. He, and Y. T. Zhu, *Appl. Phys. Lett.* **83**, 632 (2003).
- ⁸²A. Hasnaoui, H. Van Swygenhoven, and P. M. Derlet, *Science* **300**, 1550 (2003).
- ⁸³K. A. Gschneidner, *Solid State Phys.* **16**, 275 (1964).
- ⁸⁴S. R. Phillpot, D. Wolf, and H. Gleiter, *J. Appl. Phys.* **78**, 847 (1995).
- ⁸⁵A. Latapie and D. Farkas, *Scr. Mater.* **48**, 611 (2003).
- ⁸⁶E. Bonetti, E. G. Campari, L. Del Bianco, and G. Scipione, *Nanostruct. Mater.* **6**, 639 (1995).
- ⁸⁷A. M. El-Sherik, U. Erb, G. Palumbo, and K. T. Aust, *Scr. Metall. Mater.* **27**, 1185 (1992).
- ⁸⁸J. A. Zimmerman, C. L. Kelchner, P. A. Klein, J. C. Hamilton, and S. M. Foiles, *Phys. Rev. Lett.* **87**, 165507 (2001).
- ⁸⁹C. L. Kelchner, S. J. Plimpton, and J. C. Hamilton, *Phys. Rev. B* **58**, 11085 (1998).
- ⁹⁰H. Van Swygenhoven, P. M. Derlet, and A. G. Frøseth, *Nat. Mater.* **3**, 399 (2004).